

Optimized molecule supply from nozzle-based gas injection systems for focused electron- and ion-beam induced deposition and etching: simulation and experiment

V Friedli and I Utke

EMPA, Swiss Federal Laboratories for Materials Testing and Research, Laboratory for Mechanics of Materials and Nanostructures, Feuerwerkerstr. 39, CH-3602, Thun, Switzerland

E-mail: ivo.utke@empa.ch

Received 11 March 2009, in final form 1 May 2009

Published 5 June 2009

Online at stacks.iop.org/JPhysD/42/125305

Abstract

We simulated and measured near-field distributions of molecules impinging on a flat substrate from tube-based nozzles with varying exit aperture geometries (straight, bevelled and doubly perforated). Simulations were performed with the test-particle Monte Carlo approach taking into account the Knudsen number (molecular/transient flow) at the nozzle exit. Distributions were measured via thermal decomposition of $\text{Co}_2(\text{CO})_8$ molecules on a homogeneously heated substrate. For all geometries and Knudsen numbers a good match between the simulation and experiment was found. For the first time the maximum accessible molecule flux with respect to the total flux exiting the nozzle could be quantified: it is around 7% for a straight cylindrical tube, around 27% for a bevelled tube and around 32% for a doubly perforated tube, all nozzles being 300 μm distant from the substrate and having a 400 μm aperture. Optimum substrate–nozzle angles were determined and shadow effects quantified.

(Some figures in this article are in colour only in the electronic version)

1. Introduction

Gas-assisted deposition and etching with a focused electron beam (FEB) or a focused ion beam (FIB) are frequently used for three-dimensional maskless prototyping at the nanometre scale. Applications range from nanooptics (plasmon resonance structures, photonic crystals, phase shift masks), nanoelectronics (field emitters, contacts to nanotubes and wires, circuit editing), nanolithography (etch masks), scanning probe sensors with nanometre-resolution (magnetic sensors, temperature sensors, optical near-field sensors, atomic force sensors) to nanobiological applications (organelle cutting tools). For more details on the above applications, see [1]. The high number of applications is due to the flexibility imparted by the electron and ion-beam resolution in combination with the many choices of volatile molecule species which can be

used to deposit many different material compositions. These molecules reversibly adsorb (physisorption) on the substrate (planar or non-planar) and are dissociated by the very local electron or ion impact. The non-volatile fragments are deposited whereas volatile fragments are pumped away upon desorption.

Gas injection systems (GISs) with a straight cylindrical tube nozzle design are frequently used for gas-assisted deposition and etching with FEB and FIB. They can supply a high local molecule flux to the electron or ion-beam impact area on the substrate while keeping the overall chamber pressure of the microscope low enough for focused electron/ion beam operation. Moreover, substrates can be moved freely below such a GIS in contrast to environmental subchambers [2–4]. Although being in use in almost any focused beam induced deposition and etch microscope, the spatial distribution of

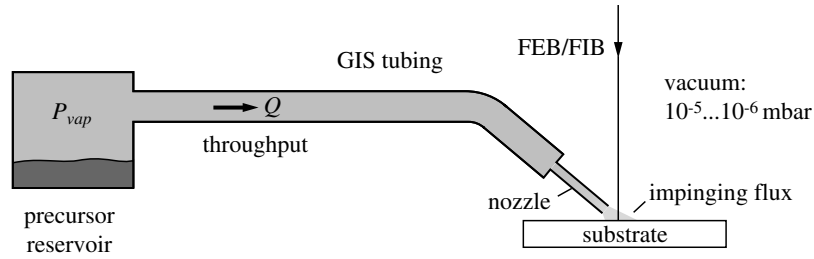


Figure 1. Schematics of a nozzle-based GIS for FEB/FIB induced processing. The precursor reservoir contains the solid, liquid or gaseous precursor. High vapour pressure precursors are dosed by mass flow controllers or needle valves which are not shown here.

the impinging molecule flux has never been quantified. Consequently, the impinging molecule flux at the point of beam impact on the substrate is missing in (almost) all the relevant literature concerning gas-assisted FEB and FIB processing and the correct interpretation of the results or their reproducibility by other groups is difficult. It is crucial to know how efficiently dissociated molecules can be replenished (refreshed) inside the irradiated area by new molecules from a GIS arrangement since this will determine the regime in which deposition or etching will proceed. The process rate and the spatial resolution of the deposit or etch hole strongly depend on whether the process is molecule-limited or electron/ion-limited [5–10]. Furthermore, the chemical composition of the deposit material [11, 12] and its internal nanocrystal/matrix structure [13, 14] both depend to a certain extent on the process regime.

A limited number of measurements of gas flux near-field distributions in rarefied flow conditions can be found in the literature. In these studies diatomic (H_2 , N_2 , CO) and noble atoms (He , Ne , Ar , Kr and Xe) were used. The experiments were based on a pressure measurement using an ionization gauge [15–17] or a mass spectrometer [18] behind a sub-millimetre-sized entrance aperture which spatially samples the flux distribution. However, the experimental complexity is large and the spatial resolution is limited to the aperture size which must allow for a measurable molecule flux.

GIS related total molecule flux measurements [19–21] and models [22] have also been studied. Attempts to determine and model the molecule flux distribution were reported recently, however, they only consider specific GIS-substrate arrangements and specific pressure ranges (flow regimes) and molecules [23–25].

In this paper we close this gap and present a simulator for gas injection (GIS simulator) which works in the molecular and transient flow regime. As an output, the impinging molecule flux distribution is obtained as a function of the nozzle geometry and the mutual arrangement between nozzle and substrate. The straight cylindrical tube nozzle and two alternative versions with modified exit apertures were evaluated. The simulations were checked against experiments. The scope of this paper focuses entirely on the gas supply and does not deal with dissociation issues by FEB/FIB impact on molecules.

2. GIS fundamentals

The basic GIS is composed of a molecule reservoir and a tubing system which connects to the exit nozzle above the substrate

(see figure 1). Optional valves and mass flow controllers can be added to control injection more quantitatively. For solid and liquid precursors the pressure in the reservoir corresponds to the vapour pressure of the molecule and for gaseous precursors, it corresponds to the gas pressure at a given temperature. Strictly speaking this is an assumption since the net flow of the molecules through the nozzle exit does not allow for equilibrium between the condensed and gaseous phases of the molecule; however, this deviation is often negligible. The vapour pressure can be controlled by the reservoir temperature. It is to be noted that possible condensation of molecules on tubing surfaces which have a lower temperature than the precursor reservoir can change the flux distribution and lead to non-reproducible results.

If no mass flow controller is used in the GIS arrangement the total throughput Q (in molecules per unit time) through the GIS can be determined by measuring the (solid) precursor mass loss Δm using a precision balance with sub-milligram resolution. After an injection period Δt the total throughput becomes $Q = (\Delta m / \Delta t) \cdot (N_a / M)$, where N_a is Avogadro's constant and M is the molar mass of the precursor molecule. The corresponding total flux J_{tot} (in molecules per unit area and unit time) at the tube nozzle exit is then derived from the inner diameter d of its exit aperture:

$$J_{tot} = 4Q / (\pi d^2). \quad (1)$$

Another important quantity, the Knudsen number Kn describes whether the molecule gas flow proceeds only with tube wall collisions (molecular flow) or in conjunction with collisions between molecules (transient flow). The Knudsen number is defined as the ratio between the mean free path between molecule collisions λ and the inner tube diameter d :

$$Kn = \lambda / d = (kT / (2^{1/2} \pi \delta^2 P)) / d. \quad (2)$$

Here k is the Boltzmann constant, T is the absolute temperature, δ is the molecule diameter and P is the pressure. As a rule of thumb, Knudsen numbers > 10 indicate that molecular flow increasingly dominates and Knudsen numbers < 10 indicate that transient flow increasingly dominates [26]. There will be a pressure gradient between the molecule reservoir and the nozzle exit to vacuum. The Knudsen number inside the reservoir is approximately obtained by inserting the static molecule vapour pressure for P . In contrast, the Knudsen number at the nozzle exit is determined mainly by the *dynamic* pressure, P_d , of the flowing gas. The static pressure at the

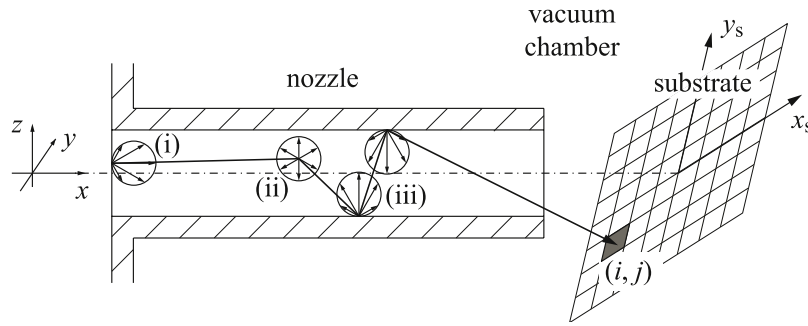


Figure 2. The molecule trajectories through the nozzle tube are traced by the following stochastic concepts: (i) Cosine point-source at tube entry. (ii) Hard sphere scattering after having travelled a free path s . (iii) Diffuse (cosine) nozzle wall scattering. The substrate is subdivided into a sampling grid for counting impinging molecules.

nozzle exit, being approximately equivalent to the chamber background pressure, $P_b < 10^{-2} - 10^{-3}$ Pa, can be neglected since typically, $P_b \ll P_d$. The dynamic pressure at the nozzle exit is straightforwardly obtained from the measured total molecule flux (1)

$$P_d = J_{\text{tot}}(2\pi MRT)^{1/2}/N_a, \quad (3)$$

where $R = 8.314 \text{ J mol}^{-1} \text{ K}^{-1}$ is the universal gas constant. Knudsen numbers stated in this paper were obtained by inserting (3) into (2).

3. The GIS simulator

Analytic solutions for the angular distribution of the exiting molecule flow are limited to long straight tubes with circular cross-sections under molecular flow ($Kn = \infty$) [27] and do not apply in the proximity of the tube exit. In the following we describe the Monte Carlo (MC) simulation algorithms we used and the nozzle designs investigated.

3.1. General

The three-dimensional GIS simulator [28] was written in C++ embedded in a graphical user interface developed in the GUI design environment provided with MatlabTM. It is based on the test-particle approach which was first introduced by Smith and Lewin [29]. Basically, molecule trajectories are computed consecutively in a large number, typically 10^6 – 10^7 molecules which transmit the nozzle into the chamber, to predict the macroscopic flow distribution on a substrate. Strictly speaking, this approach can be rigidly applied only for molecular flow conditions where molecule trajectories are indeed independent of one another since collisions occur only with the inner tube wall. However, Knudsen numbers for many precursor vapour pressures and GIS geometries indicate transient flow regimes [1]. Therefore transient molecule flow was included by simulating an intermolecular collision after the molecule reached its actual free path $s = \lambda \cdot \ln(Rn^{-1})$ [30], with λ the mean free path and Rn a uniformly distributed random number between 0 and 1. The issue in using this approach is that the mean free path distribution due to the pressure gradient between precursor reservoir and tube nozzle exit inside the tube is unknown and cannot be calculated with the

test-particle approach. A more complete approach for such cases is the direct simulation MC method [31], which computes the positions and velocities of all molecules simultaneously for discrete time steps until the steady state distribution is reached. In contrast to the test-particle method, the mean free path distribution, i.e. the pressure gradient, results as output of the direct simulation MC method. Unfortunately, this advantage has an enormous computational cost which is not practical for the GIS optimization and evaluation on today's best performing personal computers in a reasonable time. However, in this paper we prove that the test-particle method can be applied with high accuracy for flux distribution simulations on substrates using the Knudsen number (or mean free path) prevailing at the very end of the nozzle exit. It is derived from (1–3):

$$Kn = \frac{(RT/\pi M)^{1/2}}{8\delta^2(Q/d)} \quad (4)$$

and can be calculated from the measured total throughput. Outside the nozzle the Knudsen number was set to infinity, i.e. molecules followed a straight trajectory after their last collision inside the tube nozzle until they hit the substrate (no molecular collisions outside the tube). This assumption proved meaningful with respect to results from the direct simulation MC method and our experiments [32], see section 5.3.

3.2. Algorithms

The simulation of a molecule trajectory starts at the entrance surface of the nozzle tube (see figure 2). Molecules are uniformly generated over this surface and 'start' with a cosine angular velocity distribution [33]. The trajectory of the molecule is then determined by intramolecular collisions and collisions with the inner tube wall. The trajectory is finished when the molecule escapes from the tube either through the entrance surface (physically this means it is backscattered into the source reservoir) or when it transmits through the exit surface. The transmitted molecules are spatially mapped on the substrate surface and the locally impinging flux J is normalized with respect to J_{tot} . The scattering of the molecules at the substrate surface and their consecutive trajectories inside the vacuum chamber are not taken into account.

We now discuss fundamental assumptions (and prove their validity) involved in the collision algorithms and the pressure distribution inside the flow.

(i) In our simulations diffuse scattering of molecules from the inner tube walls is applied. This means that the desorption direction of the molecule is independent of the direction of incidence. In other words, the molecule desorption from the surface occurs randomly after negligible surface diffusion. The differential angular velocity probability, p , written in terms of the polar and azimuthal angles θ and ϕ , respectively, is described by the well-known cosine law

$$dp = \frac{1}{\pi} \cos \theta \sin \theta d\theta d\phi. \quad (5)$$

For microscopically rough surfaces the diffuse scattering law is in many cases an adequate description which is well-established theoretically and experimentally (for references see the textbook by Lafferty [30]). Thomson and Owens pointed out that a combination of diffuse and specular reflection of the gas from the tube surface in some conditions matches better with the experimental results [34]. We saw that the agreement with our experiments is reduced when adding a specular term.

(ii) Chemisorption of molecules at the inner tube walls can be included through an uptake coefficient defined as the probability of sticking forever to the tube upon a collision with its wall. The MC simulations show that the molecule flux was reduced and collimated by chemisorption, since the molecules transmitting without wall collisions now dominate the angular flux distribution while the molecules having wall collisions are ‘lost’ by uptake [29]. So far the practical importance of chemisorption inside the GIS was outlined only for the molecule $\text{Fe}(\text{CO})_5$, where, as a result, the exit flux composition was enriched with CO molecules which dissociated from the parent molecule, leaving Fe on the tube wall [35]. It is to be noted that chemisorption can change with increasing coverage by chemisorbed molecules, simply due to the fact that the chemisorbed material has different ‘interaction’ properties with the precursor molecule than the initial tube material. It can favour physisorption (and reduce the initial uptake) or lead to increased auto catalytic dissociation (and increase the initial uptake). Which of these processes will dominate for a specific molecule must be investigated experimentally since no data are available in the literature. Uptake factors manifest as mass and colour changes in the tubing system and any uptake factor can be readily introduced into the GIS simulator code. For $\text{Co}_2(\text{CO})_8$ we measured that chemisorption is less than 3% which does not result in an observable change in our simulated flux profiles.

(iii) Scattering during intermolecular-collisions was simulated according to the hard sphere model. It is assumed that molecules are hard elastic spheres of diameter δ with a total collision cross-section of $\sigma = \delta^2\pi$. In view of the random orientation and the large number of collisions it is reasonable to assume a spherically symmetric geometry even for polyatomic molecules. In the literature, modelling with more realistic collision cross-sections is well documented [31] but beyond the scope of this paper. The differential angular velocity probability upon an intermolecular hard sphere collision is isotropic in all directions as seen from the molecule’s centre of mass. This is a good approximation and it has been found

that the observable consequences of changes in the scattering law are generally very small [31]. Accordingly, the velocity direction after an intermolecular collision is independent of the initial direction of the molecule and colliding molecules depart towards the tube exit or the entrance with a 1 : 1 probability.

(iv) Transient flow simulations were performed setting the mean free path $\lambda = d \cdot Kn$ inside the entire nozzle. Since Kn is defined by (4), it thus considers the flow regime prevailing near the end of the nozzle exit. We verified by simulations that it is the proportion between wall- and intermolecular-collisions near the nozzle exit that finally governs the angular distribution of the molecules exiting the nozzle. This result also led to the computational concept of a reduced nozzle (tube) length to decrease the computation time. A tube with reduced length L_r yields approximately the same simulation results for impinging molecule distributions on a substrate compared with a long full-length nozzle. However, the reduction in computational effort is remarkable since the probability of the molecule transmission through a nozzle of reduced length is drastically increased compared with the nozzles of 100 mm length used in today’s GISs. The critical reduced nozzle length L_r was determined by a series of simulations where the length of the nozzle was varied while its diameter was fixed. For molecular flow conditions the spatial distribution of the impinging molecules on the substrate is insignificantly altered for nozzle lengths $L_r > 15d$. For transient flow conditions the critical reduced nozzle length depends on λ and $L_r = 3 \dots 5\lambda$. According to the kinetic gas theory this corresponds to a fraction $1 - e^{-L_r/\lambda} = 95 \dots 99\%$ of molecules that have suffered an intermolecular collision within the distance L_r . This illustrates that intermolecular collisions have a screening effect for molecules transmitting towards the nozzle exit. Also, the consequence from this simulation series is that the pressure gradient inside the nozzle between the reservoir and vacuum side only marginally influences the molecule distribution on the substrate.

3.3. Simulated nozzle designs

The following nozzle designs were simulated: a straight tube nozzle, a bevelled nozzle with a FEB/FIB access hole and a doubly perforated end-closed horizontal nozzle as shown in figure 3. The reference system on the substrate (x_s, y_s, z_s) has its x_s -axis always parallel to the normal projection of the tube axis to the substrate. Note that each design has a specific reference origin.

4. Experimental

Our experimental approach for the characterization of the precursor flux distribution relies on the thermal decomposition of the impinging precursor molecules on a heated substrate. In the precursor mass-transport limited deposition regime the shape of the deposited material represents the locally impinging flux on the substrate. In the following we refer to the method as local chemical vapour deposition (CVD).

Our GIS consisted of the precursor reservoir made of Teflon and metal tubings which connected the reservoir to the

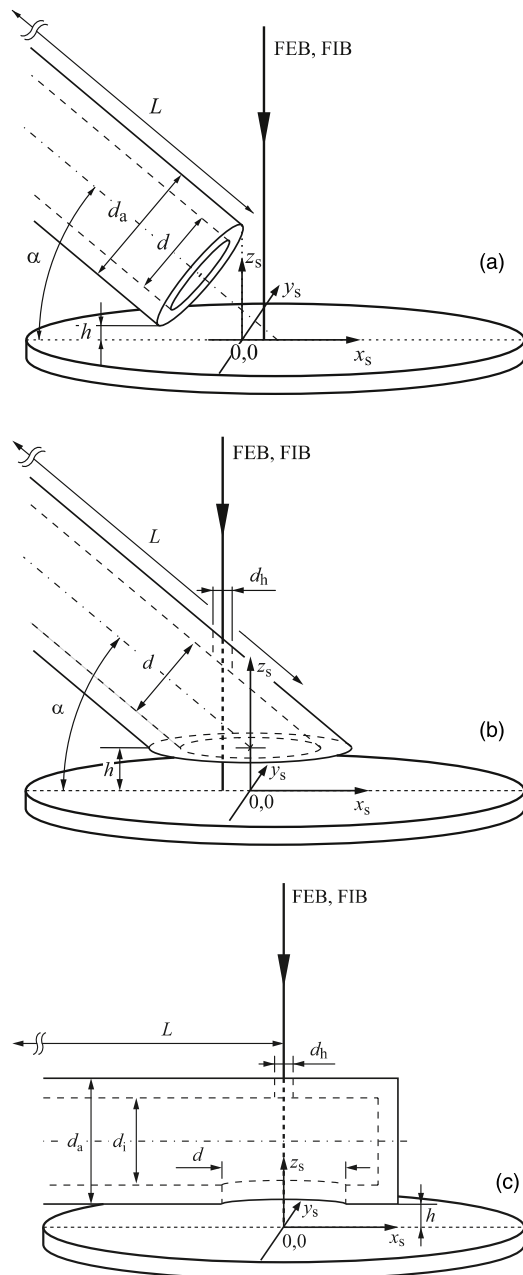


Figure 3. Reference systems and geometrical arrangements for MC simulations. FEB/FIB access is indicated. (a) Straight tube design. Origin defined by upper tube edge projection. (b) Bevelled nozzle with access hole for FEB/FIB passage. (c) Doubly perforated nozzle with FEB/FIB access hole and co-aligned precursor molecule exit hole. The tube is closed at the end. Note that $d \gg d_h$.

stainless steel nozzle. The GIS tubings, reservoirs and nozzles were assembled from standard components used for medical applications. The roughness average of the inner tube walls is specified as 0.8–1.6 μm . This modular setup enabled the GIS nozzle to be easily interchanged while keeping the rest of the assembly unchanged. The differing nozzle geometries discussed above were fabricated by manual grinding and by laser drilling of additional holes. The GIS setup was enclosed entirely inside a custom-built reactor chamber. The chamber was evacuated by a turbo-molecular pump backed by a rotary pump. Background pressures in the order of $3 \dots 5 \times 10^{-3}$ Pa

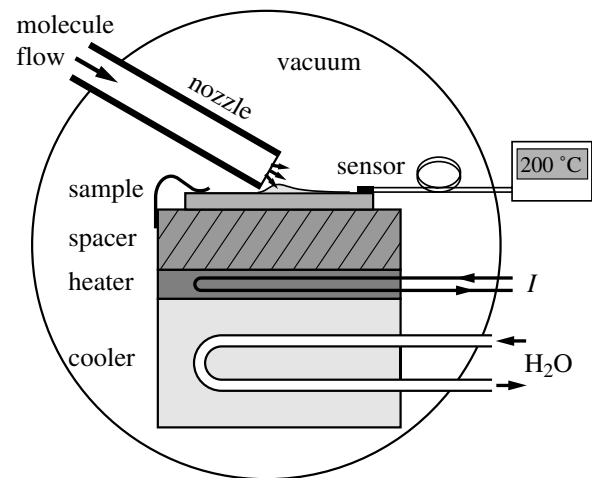


Figure 4. Schematics of the reactor setup for the experimental determination of the precursor gas flow distribution impinging on a plane substrate. Real time stereo-microscope observation proceeded along the 'paper normal'. The sample heater was mounted onto a xyz -stage with micrometre-positioning accuracy. The spacer element between the resistive heater element and the sample acted as a temperature homogenizer. A thermo-couple element (type K) sensed the temperature on the top surface of the sample.

were routinely reached.

Transparent windows were used so that the distance and angle between the nozzle and the substrate could be observed and measured with an optical microscope (Leica MZ16 A Stereomicroscope). Furthermore, the local CVD process could be followed in real time such that the deposition process could be stopped at any desirable thickness.

The heating setup is shown in figure 4. Substrate heating was achieved with a boron nitride resistive heating element. It was mechanically attached to the sample holder (movable in x - y - z) which was kept at room temperature by a circulating water flow. The substrate samples with a typical size of $2 \times 2 \text{ cm}^2$ were held in place by a stainless steel spring sheet on a polished stainless steel or copper plate which was in direct contact with the resistive heater. This spacer metal piece increased the thermal contact to the substrate and homogenized the temperature gradients. The substrate temperature was measured by a thermo-couple (type K) which was mechanically clamped to the substrate by a spring sheet. This heating setup typically reached the substrate temperatures of 200°C within some minutes. The temperature stability was manually controlled within $\pm 5^\circ\text{C}$. During temperature stabilization the sample holder with the heated substrate was kept distant from the GIS to avoid GIS heating. Only for local CVD was the nozzle moved close to the substrate (within $100 \mu\text{m}$), see figure 4. Except for one experiment (see figure 5(b)) all of the depositions using $\text{Co}_2(\text{CO})_8$ were carried out at a constant substrate temperature of 200°C . Several depositions (a maximum of three within <20 min) on the same substrate were made consecutively.

The precursor $\text{Co}_2(\text{CO})_8$ (hexane stabilized, Aldrich, CAS: 10210-68-1) was used for the local CVD experiments due to its low CVD temperature of 150°C – 400°C [36]. However, at 60°C noticeable CVD was observed, presumably

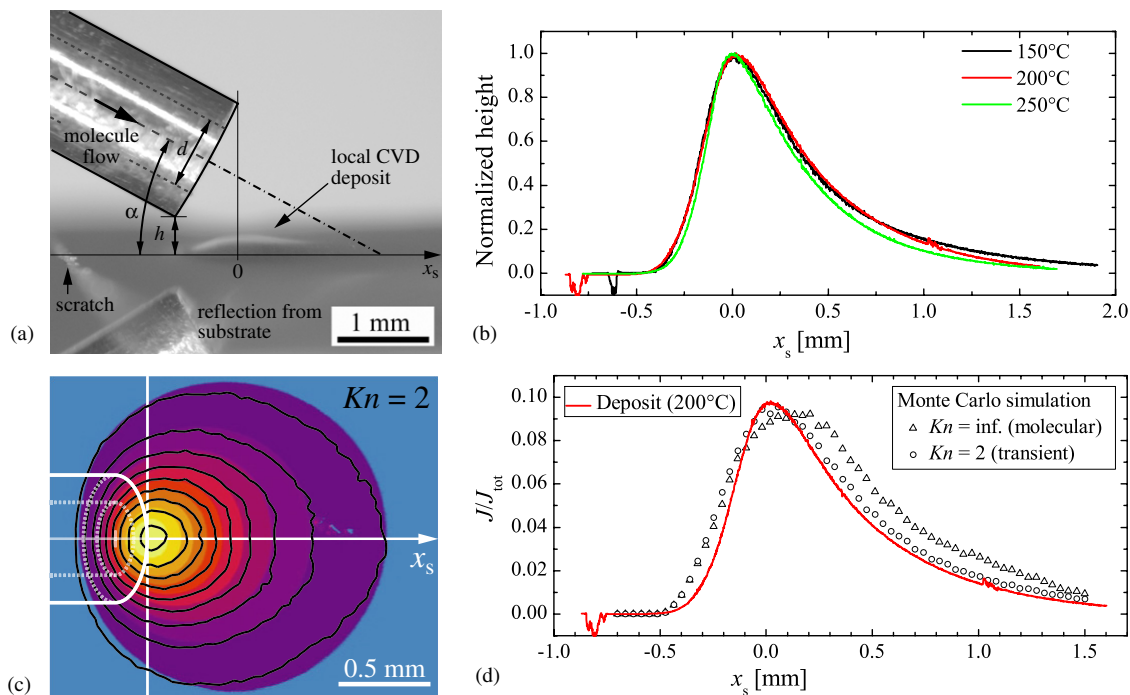


Figure 5. (a) Stereo-microscope image of the nozzle–substrate configuration during CVD. The inner tube diameter d and the tube axis are indicated ($d = 400 \mu\text{m}$, $d_a = 700 \mu\text{m}$, $\alpha = 30^\circ$, $h = 220 \mu\text{m}$). The very nozzle edge as seen by a zero tilt impinging electron beam defines $x_s = y_s = 0$. (b) Height profiles of the CVD deposits measured along x_s (at $y_s = 0$). (c) Measured topography (filled contours) of the 200°C deposit superposed with simulated isoflux contours (dark lines) for transient flow with $Kn = 2$. The tube position and the reference system are also indicated. (d) Simulations of impinging molecule flux along x_s (at $y_s = 0$) for molecular ($Kn = \infty$) and transient flow ($Kn = 2$). The measured height profile (solid line) from the 200°C deposit shown in (c) is superposed.

due to autocatalysis [37] which is common to a number of metal carbonyl molecules [38]. The vapour pressure of $\text{Co}_2(\text{CO})_8$ was studied by Garner *et al* [39]. Their reported temperature dependence of the total vapour pressure was $\log(P_{\text{vap}}[kPa]) = -4402/T + 12.8$, which corresponds to $P_{\text{vap}} = 13.4 \text{ Pa}$ at 27°C, as was used in this work.

Vertical scanning optical profilometry measurements with a WykoTM NT1100 profilometer were performed to determine the topography after local CVD. The deposits had lateral dimensions in the order of 1...2 mm and thickness $< 100 \mu\text{m}$. The reliability of the optical measurements and base-plane corrections were verified by contact mode stylus profiles.

5. Results and discussion

5.1. Straight tube nozzle

The straight tube nozzle is the conventional design used in most GIS systems. Figure 5(a) shows an optical image of the tube–substrate configuration in our reactor chamber. The microscope observation axis was arranged nearly perpendicular to the tube axis–substrate normal plane to allow projection-free distance measurements in the microscope images. A final deposit with a maximum height in the order of 50...100 μm is observed on the substrate after 12...15 min of local CVD. The precise determination of the tube–substrate height h and the nozzle–substrate angle α is possible when using the nozzle mirror image from the polished substrate. It should be noted that the tube nozzle position (x_s -position)

could be precisely determined from a scratch in the substrate (see figure 5(a)).

The deposit shapes obtained at substrate temperatures of 150, 200 and 250°C, as shown in figure 5(b), were very similar. At the position of maximum impinging flux we measured deposition rates of 4 $\mu\text{m min}^{-1}$, 6 $\mu\text{m min}^{-1}$ and 8 $\mu\text{m min}^{-1}$ at substrate temperatures of 150°C, 200°C and 250°C, respectively. This temperature dependence is attributed to an increasing molecule flux due to radiative heating of the precursor reservoir. We measured a 7 K temperature increase in the GIS, held initially at 30°C, within 40 min during the three successive experiments. This increases the vapour pressure (and thus the total flux) of $\text{Co}_2(\text{CO})_8$ by a factor of 1.5 (from 30°C to 33.5°C) and 2.1 (from 30°C to 37°C) using the temperature dependence mentioned before. These ratios are also found for the above deposition rates $6/4 = 1.5$ and $8/4 = 2$, respectively. Since the topography of all deposits scaled linear with the flux in the temperature range 150°C–250°C it can be concluded that our local CVD proceeded in the mass limited regime. Furthermore, the observed constant growth rate rules out the relevance of temporary surface temperature inhomogeneities due to substrate cooling by the molecule flux or due to a low thermal conductivity of the deposited material. Energy dispersive x-ray spectroscopy measurements revealed that the deposit composition was $\text{Co}_{0.8}\text{C}_{0.1}\text{O}_{0.1}$, while the SEM images showed the morphology of the deposits to be sheet-like grains.

Figure 5(c) shows that transient flow simulations with $Kn = 2$, obtained from (4), with $\delta_{\text{Co}_2(\text{CO})_8} = 0.7 \text{ nm}$ and

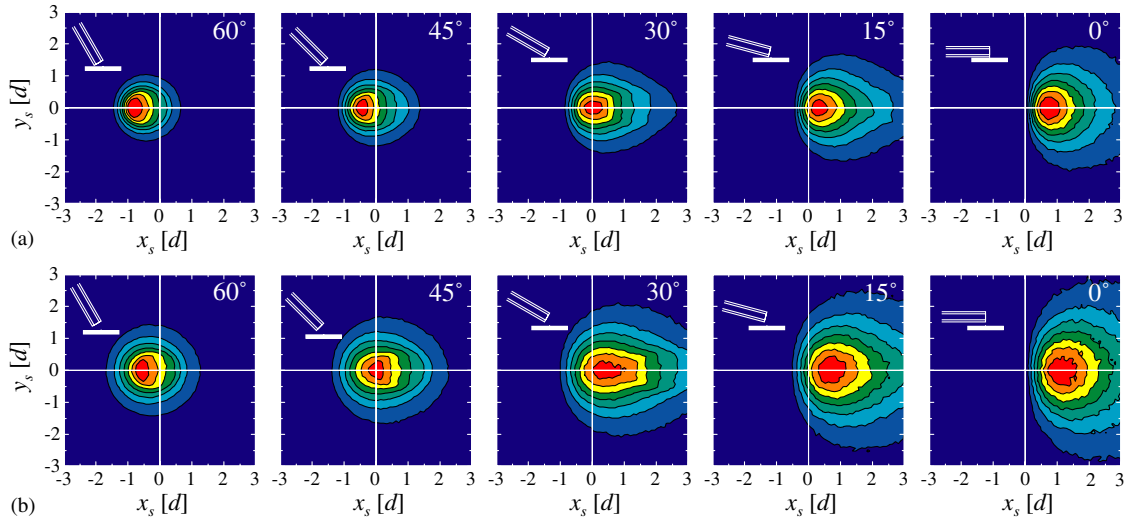


Figure 6. Simulated isoflux contours (molecular flow, $Kn = \infty$) at varying incidence angles and vertical distances (see insets for configuration). The nozzle obscures the substrate at $x_s \leq 0$ for the FEB/FIB normally incident on the substrate plane. Nozzle dimensions: $L = 15d$, $d_a = 1.75d$. Vertical nozzle–substrate distance: (a) $h = 0.25d$, (b) $h = 0.75d$. For a tube nozzle with $d = 400 \mu\text{m}$ ($d_a = 700 \mu\text{m}$) this results in a length $L = 6 \text{ mm}$ and $h = 100 \mu\text{m}$ and $300 \mu\text{m}$, respectively. For the absolute flux scale, see figure 7.

$J_{\text{tot}} = 2 \times 10^{18} \text{ cm}^{-2} \text{ s}^{-1}$ (from measurements), match the three-dimensional deposit topography very well. The good match between this simulation and the experiment is also obvious in the corresponding profile shown in figure 5(d): the simulated full width at half maximum (FWHM) matches the experiment to better than 20% and the deviation in the simulated flux value is $< 8\%$ in the FEB/FIB accessible region, $x_s > 0$. In contrast, the molecular flow simulated profile deviates considerably. That (4) is a very good estimate for input in our MC simulations is also supported by our previous experiments using the precursor $\text{Rh}_2\text{Cl}_2(\text{PF}_3)_4$. The calculated corresponding Knudsen number of 10 (molecular flow) used as an input into the simulations also showed a very good match with the deposit topography [25]. Generally, the shape of the (simulated) impinging flux profiles is strongly sensitive to variations of Kn between 1 and 10, i.e. while changing from transient to molecular flow.

The slight decrease in the FWHM of the 250°C deposit in figure 5(b) is due to a temperature increase in the reservoir to 37°C . This basically doubles the vapour pressure which is equivalent to a reduction in the initial Knudsen number 2 (at 30°C) by a factor of 0.5. Indeed the simulations using $Kn = 1$ (not shown in figure 5) matches this trend.

We would like to point out that the agreement, i.e. peak position, FWHM and accuracy of the molecule distribution, between our simulations and the related experiments is very good compared with previous published attempts [21, 23]. For example, a continuum approach (Navier–Stokes) [23] for a straight tube nozzle design resulted in a deviation of nearly a factor 2 between the FWHM of the simulated and experimental curve.

5.2. Optimum straight nozzle configuration

Having verified the very good agreement between our GIS simulations and experiments we proceed now to simulations

which give guidelines for the optimum position of the straight tube nozzle relative to the substrate in terms of the maximum accessible precursor flux and uniformity within the FEB/FIB processing field. We considered a tube with $L = 15d$, exceeding the critical reduced length, as explained in section 3.2.

In figure 6, two-dimensional isoflux contour patterns are presented for a vertical tube–substrate distance of $h = 0.25d$ and $0.75d$ and a tube incidence of $\alpha = 60, 45, 30, 15, 0^\circ$. The reference origin was chosen as shown in figure 3(a), i.e. the obscured substrate region for the FEB/FIB (due to the nozzle) always falls together with $x_s \leq 0$. It can readily be deduced that at large tube incidence angles, the flux peak is inaccessible for the FEB/FIB. The ‘accessible’ flux profiles along the tube axis are summarized in figure 7. Close to the nozzle, a maximum flux is produced for large incidence angles, whereas at low incidence angles the flux level is strongly reduced even for the flux peaks situated at $x_s > 0$. Within the presented range for $h = 0.25d \dots 0.75d$ the accessible peak flux is maximal for 60° incidence, almost 20% of the total effusing flux, while it has the strongest non-uniformity. Optimum uniformity at high flux levels, around 7% to 9%, is predicted at $15 \dots 30^\circ$ incidence depending on h . At incidence $\alpha \rightarrow 0^\circ$ a lower flux level results and is again strongly non-uniform within the simulated range.

In conclusion, if a uniform flux within the accessible region is to be ensured, a tube incidence angle between 15° and 30° is favourable in the molecular flow regime at $h = 0.25d \dots 0.75d$. These results are scalable with tube dimensions as long as molecular conditions prevail. In transient conditions the same qualitative trend is predicted by our simulations; however, simulations are case specific due to the corresponding Knudsen number.

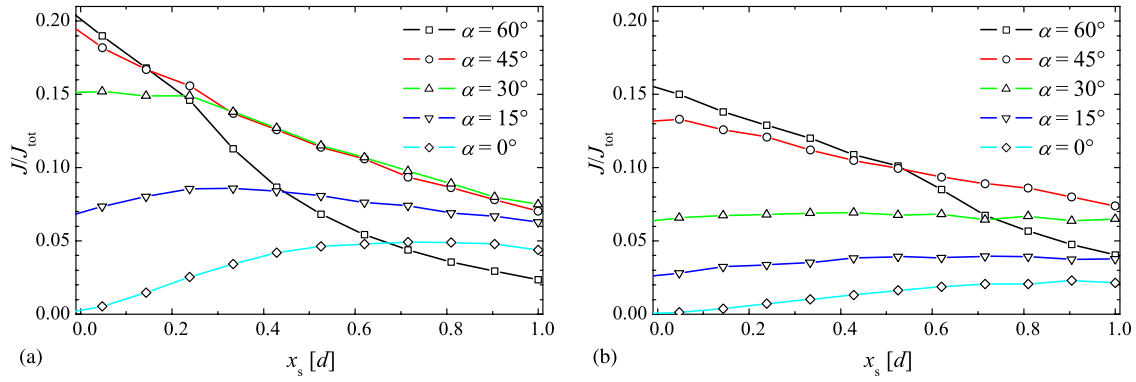


Figure 7. Normalized molecular impinging flux profiles on the substrate along x_s at ($y_s = 0$) corresponding to simulations in figure 6. J_{tot} is the total flux effusing from the tube exit surface. Values at $x_s < 0$ are not shown, since these locations are not accessible by the FEB/FIB. Nozzle dimensions: $L = 15d$, $d_a = 1.75d$. Vertical nozzle–substrate distance: (a) $h = 0.25d$, (b) $h = 0.75d$.

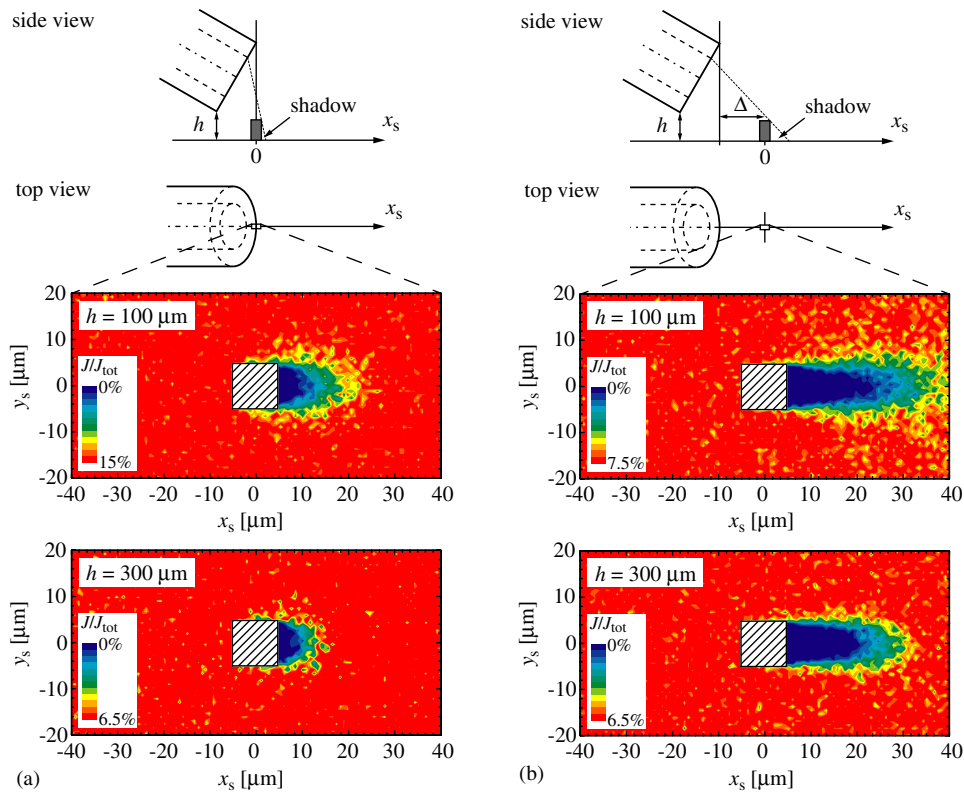


Figure 8. Side and top view illustrations of GIS nozzle–substrate arrangement with the corresponding simulated isoflux contours of impinging molecule flux J/J_{tot} around an obstacle (hatched box) of $20 \mu\text{m}$ height and $10 \times 10 \mu\text{m}^2$ footprint (the obstacle is scaled 10 : 1 in the side view illustration). The simulation was performed under molecular flow conditions, for nozzle–substrate heights $h = 100 \mu\text{m}$ and $h = 300 \mu\text{m}$, and a tube incidence angle $\alpha = 30^\circ$. The GIS nozzle dimensions were $d = 400 \mu\text{m}$ ($d_a = 700 \mu\text{m}$) with a length $L = 4 \text{ mm}$. (a) The obstacle is located closest to the nozzle. (b) The obstacle is located a distance $\Delta = 400 \mu\text{m}$ away from the nozzle.

5.3. Shadow effects in straight nozzle configuration

The shadow effects due to a three-dimensional obstacle located on the substrate are shown quantitatively in figure 8. The shaded areas with zero molecules impinging are strongly dependent on the obstacle geometry and mutual positions of the obstacle and nozzle. Here a relatively large obstacle of $20 \mu\text{m}$ height and $10 \times 10 \mu\text{m}^2$ area was chosen to highlight the shadow effects. The FEB deposits are one to two orders of magnitude smaller in lateral dimensions.

The shadow effects lead to reduced FEB/FIB deposition rates on the shaded surface due to a reduced molecular

coverage. It has been seen that during FEB and FIB induced deposition of micro- and nanostructures, different growth rates were obtained when scanning the beam towards different directions relative to the impinging flux [40, 41]. In practice, surface diffusion can supply additional molecules to the area which is shaded from directly impinging flux due to the concentration gradient. The critical dimension of surface diffusion is the molecular diffusion path $(D\tau)^{1/2}$, where D is the diffusion coefficient and τ is the residence time of adsorption of the molecule on the surface. Inserting typical values, $\tau = 1 \text{ ms}$ and $D = 3 \times 10^{-8} \dots 4 \times 10^{-7} \text{ cm}^2 \text{ s}^{-1}$

for copper hexafluoroacetylacetonate molecules [9] yields an estimation of the average diffusion path length of 50...200 nm. Generally, the shadowed regions will be replenished when their sizes are comparable to the average diffusion path and the molecule coverage will be homogenized by surface diffusion. This is probably the reason why homogeneous small-diameter pillars can be deposited with rotational symmetry and high aspect ratios. When deposited pillar diameters came close to 1 μm , non-rotational symmetries as well as internal structural inhomogeneities were observed [14].

We can now also quantify another possible source for molecule replenishment of shadowed regions, the molecule contribution from the operating background pressure. For example, using a straight tube nozzle of 6 mm length and 0.6 mm inner diameter we measured a total injected flux $J_{\text{tot}} = 9 \times 10^{16} \text{ cm}^{-2} \text{ s}^{-1}$ and a background chamber pressure rise to $P_b = 10^{-3} \text{ Pa}$ during gas injection of the molecule copper hexafluoroacetylacetonate $\text{Cu}(\text{hfa})_2$ at room temperature. Inserting P_b into (3) results in a background flux impinging on the substrate of $J_b = 7 \times 10^{14} \text{ cm}^{-2} \text{ s}^{-1} \approx 0.4 \text{ monolayers s}^{-1}$ of copper hexafluoroacetylacetonate molecules (molecule size 0.6 nm^2). The injected molecule flux impinging on the substrate for various nozzle–substrate arrangements can be found from figure 7: choosing a tube position of 450 μm above the substrate at an angle of 30° gives a local impinging flux $J = 0.07 \cdot J_{\text{tot}} \approx 4 \text{ monolayers s}^{-1}$ from the nozzle. Thus the background contribution is 10% in this arrangement. For precursors with higher vapour pressures and correspondingly higher total injected flux the background contribution would tend to vanish provided the same GIS arrangement and background pressure. It should be noted that for a 60 mm long tube the total injected flux would decrease by a factor of 10 due to the inverse scaling of the throughput with the tube length [30]. Then background contribution and injected flux would become comparable.

Another source of molecule replenishment, the intermolecular gas-phase scattering of molecules desorbing from the substrate surface, must be considered. It cannot be quantified by our simulation model since we assume no molecular collisions outside the tube. However, with the direct simulation MC method [31] this contribution can be quantified. Simulating a typical (high) total flux of $2 \times 10^{18} \text{ cm}^{-2} \text{ s}^{-1}$ of $\text{Co}_2(\text{CO})_8$ molecules leaving the nozzle tube ($d = 600 \mu\text{m}$, $d_a = 900 \mu\text{m}$ and $L = 3 \text{ mm}$) and impinging on a 350 μm distant substrate under an incidence angle of 30° results in a maximum local impinging flux of $J = 3 \times 10^{17} \text{ cm}^{-2} \text{ s}^{-1} \approx 1200 \text{ monolayers s}^{-1}$ (molecule size 0.4 nm^2) and a mean free path between molecule collisions of $\lambda \approx 1 \text{ mm}$ at the tube exit and $\lambda > 8 \text{ mm}$ near the substrate. Consequently, gas-phase scattering outside the tube and above the substrate is negligible.

5.4. Alternative nozzle designs

Alternative nozzle geometries are inspired by the search for high and homogeneously impinging local flux at the lowest total throughput, i.e. at the lowest pressure load for the

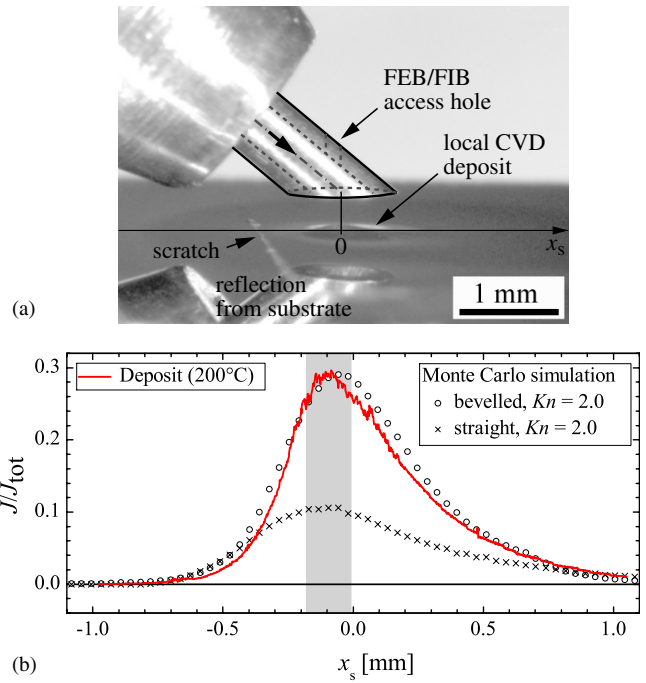


Figure 9. Local CVD experiments with bevelled nozzle. (a) Optical image of the nozzle–substrate configuration. The nozzle geometry is pointed out by an overlay. (b) Experimental and simulated profiles along x_s (at $y_s = 0$). The shaded area indicates the access hole position as seen by a zero tilt impinging electron beam. Simulations were performed with $Kn = 2$ and nozzle dimensions of $L = 4.16 \text{ mm}$, $d = 400 \mu\text{m}$, $d_a = 700 \mu\text{m}$, $d_h = 170 \mu\text{m}$. Nozzle–substrate configuration: $\alpha = 40^\circ$, $h = 287 \mu\text{m}$. For comparison, the simulated profile of a straight nozzle with equivalent tube axis, dimensions and nozzle–substrate configuration is plotted.

microscope chamber. The nozzle designs with a FEB/FIB access hole depicted in figures 3(b) and (c) can guide the molecule flux much closer to the substrate and consequently minimize molecule losses due to the divergent nature of effusion. Furthermore, for the doubly perforated closed-end nozzle the impinging molecule flux becomes isotropic, which avoids shadow effects. Unwanted secondary electron emission at the GIS nozzle by substrate scattered electrons could be minimized by biasing with an electrostatic potential. Alternatively, a larger distance between nozzle and substrate would also decrease the effects of secondary electron emission from the GIS nozzle.

Figures 9 and 10 summarize local CVD experiments with the precursor $\text{Co}_2(\text{CO})_8$ and the alternative GIS nozzle designs. The height profiles of the deposits along x_s (at $y_s = 0$) are superposed with flux simulations in transient conditions. For the bevelled nozzle design in figure 9, total flux measurements were comparable to the straight tube nozzle design and we used the Knudsen number $Kn = 2$ for this simulation. A very good agreement with the experiment can be seen: although the peak position is slightly offset in our simulations, the simulated FWHM corresponds within 12% to the FWHM of the deposit and deviations of the simulated flux values are $<10\%$ inside the FEB/FIB accessible region (access hole). Under the present conditions, the FEB/FIB access hole had no significant influence on the flux distribution as was confirmed

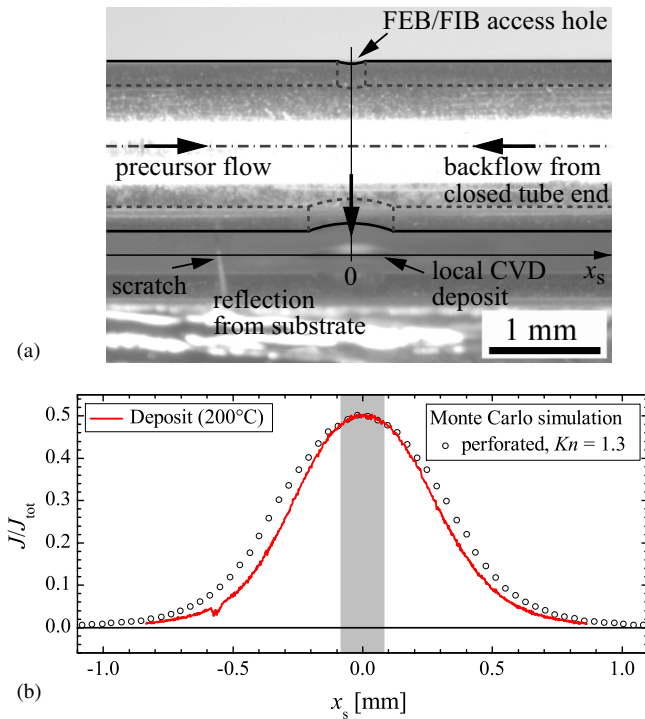


Figure 10. Local CVD experiments with perforated nozzle. (a) Optical image of the nozzle-substrate configuration. The nozzle geometry is pointed out by an overlay. (b) Experimental and simulated profiles along x_s (at $y_s = 0$). The shaded area indicates the access hole position as seen by a zero tilt impinging electron beam. Simulations were performed with $Kn = 1.3$ (within the tube) and a nozzle geometry of $L = 10$ mm, $d_i = 1.07$ mm, $d_a = 1.5$ mm, $d = 640$ μ m, $d_h = 160$ μ m. Nozzle-substrate configuration: parallel, $h = 330$ μ m. Note the J/J_{tot} axis scale with respect to figures 5(b) and 9(b).

by both the simulation and the experiment. Compared with a straight tube nozzle approximately three times higher molecule flux can be achieved and accessed with a bevelled nozzle at the same throughput (see figure 9(b)).

The experiments and simulations with the doubly perforated tube, closed at one end, are summarized in figure 10. This geometry is advantageous if isotropic flux to the site of processing is required in order to avoid the shadowing effects discussed in section 5.3. According to our total flux measurements with this nozzle design we calculated $Kn = 1.3$ using (4). The simulated impinging local flux again matches well the experimental profile (see figure 10(b)). The peak position is perfectly matched and the simulated FWHM deviates <16% from the experiment.

Table 1 compares simulations of the maximum accessible impinging flux for the three nozzle geometries. The inner diameter was kept constant for the three nozzles.

The figure of merit is given in percentage of J_{max}/J_{tot} of a straight tube nozzle. It is evident that the highest accessible molecule flux is achieved with the doubly perforated nozzle design. This becomes especially important when low vapour pressure precursors are to be supplied. Furthermore, the rotational symmetry of such a nozzle design prevents shadow effects and results in more homogeneous three-dimensional deposits.

Table 1. Comparison of simulated local impinging flux at a fixed nozzle-substrate distance h for three nozzle geometries. The nozzle diameter was set to $d = 400$ μ m for all geometries, the remaining dimensions and Knudsen numbers are identical to figures 5, 9 and 10. J_{max} is the maximum accessible flux with a zero tilt incident electron or ion beam. The percentages give the enhancement of maximum accessible flux with respect to the straight nozzle design.

| h (μ m) | J_{max}/J_{tot} | | |
|----------------|--------------------------|--------------------------|--------------------------|
| | Straight | Bevelled | Perforated |
| 100 | 0.15 (100%) | 0.70 (460%) | 0.81 (540%) |
| 300 | 0.07 (100%) ^a | 0.27 (390%) ^b | 0.32 (460%) ^c |

^a The value deviates from the maximum accessible flux in figure 5(d) due to a $1.36\times$ increased GIS-substrate height h/d .

^b The value deviates from the maximum accessible flux in figure 9(b) due to a $1.05\times$ increased GIS-substrate height h/d .

^c The value deviates from the maximum accessible flux in figure 10(b) due to a $1.45\times$ increased GIS-substrate height h/d .

6. Conclusions

A MC simulation approach for rarefied gas flows was adapted to the GISs used for FEB/FIB processing. The simulations for three nozzle designs related very well to the experimentally determined molecule flux distributions. The use of bevelled and perforated nozzles increases the accessible flux to the FEB/FIB by up to a factor of 4.6 . . . 5.4 keeping the total molecule throughput injected into the vacuum chamber constant.

Presently, the applicability of the presented GIS simulator (download from <http://www.empa.ch/GISSimulator>) is experimentally verified for Knudsen numbers >1. The results obtained from our studies established the computation-efficient test-particle MC approach as a simulation tool to predict local gas flux distributions in the context of gas-assisted FEB/FIB induced processing. In principle, the simulation should also deliver correct results for more transient conditions, i.e. for Knudsen numbers down to approximately 0.1 or even lower. It was beyond the scope of this paper to experimentally verify this pressure region.

Acknowledgments

The authors thank Claude Amendola, EPF Lausanne, for Laser drilling of holes into nozzles and Severin Waldis, IMT, Neuchâtel for vertical scanning optical profilometry measurements. Financial support is acknowledged from the EU project NanoHand.

References

- [1] Utke I, Hoffmann P and Melngailis J 2008 Gas-assisted focused electron beam and ion beam processing and fabrication *J. Vac. Sci. Technol. B* **26** 1197–276
- [2] Folch A, Servat J, Esteve J, Tejada J and Seco M 1996 High-vacuum versus “environmental” electron beam deposition *J. Vac. Sci. Technol. B* **14** 2609–14

- [3] Matsui S and Mori K 1984 New selective deposition technology by electron-beam induced surface-reaction *Japan. J. Appl. Phys. Part 2-Lett.* **23** L706–L8
- [4] Ochiai Y, Shihoyama K, Shiokawa T, Toyoda K, Masuyama A, Gamo K and Namba S 1986 Characteristics of maskless ion-beam assisted etching of silicon using focused ion-beams *J. Vac. Sci. Technol. B* **4** 333–6
- [5] Lassiter M G and Rack P D 2008 Nanoscale electron beam induced etching: a continuum model that correlates the etch profile to the experimental parameters *Nanotechnology* **19** 455306
- [6] Randolph S J, Fowlkes J D and Rack P D 2006 Focused, nanoscale electron-beam-induced deposition and etching *Crit. Rev. Solid State Mater. Sci.* **31** 55–89
- [7] Smith D A, Fowlkes J D and Rack P D 2008 Understanding the kinetics and nanoscale morphology of electron-beam-induced deposition via a three-dimensional Monte Carlo simulation: the effects of the precursor molecule and the deposited material *Small* **4** 1382–9
- [8] Smith D A, Fowlkes J D and Rack P D 2008 Simulating the effects of surface diffusion on electron beam induced deposition via a three-dimensional Monte Carlo simulation *Nanotechnology* **19** 415704
- [9] Utke I, Friedli V, Purrucker M and Michler J 2007 Resolution in focused electron- and ion-beam induced processing *J. Vac. Sci. Technol. B* **25** 2219–23
- [10] van Dorp W F and Hagen C W 2008 A critical literature review of focused electron beam induced deposition *J. Appl. Phys.* **104** 081301
- [11] Hoyle P C, Ogasawara M, Cleaver J R A and Ahmed H 1993 Electrical-resistance of electron-beam-induced deposits from tungsten hexacarbonyl *Appl. Phys. Lett.* **62** 3043–5
- [12] Utke I, Friedli V, Michler J, Bret T, Multone X and Hoffmann P 2006 Density determination of focused-electron-beam-induced deposits with simple cantilever-based method *Appl. Phys. Lett.* **88** 031906
- [13] Utke I, Bret T, Laub D, Buffat P, Scandella L and Hoffmann P 2004 Thermal effects during focused electron beam induced deposition of nanocomposite magnetic-cobalt-containing tips *Microelectron. Eng.* **73–74** 553–8
- [14] Utke I, Michler J, Gasser P, Santschi C, Laub D, Cantoni M, Buffat P A, Jiao C and Hoffmann P 2005 Cross section investigations of compositions and sub-structures of tips obtained by focused electron beam induced deposition *Adv. Eng. Mater.* **7** 323–31
- [15] Adamson S and McGilp J F 1986 Measurement of gas flux distributions from single capillaries using a modified, UHV-compatible ion gauge, and comparison with theory *Vacuum* **36** 227–32
- [16] Buckman S J, Gulley R J, Moghbelalhossein M and Bennett S J 1993 Spatial profiles of effusive molecular-beams and their dependence on gas species *Meas. Sci. Technol.* **4** 1143–53
- [17] Rugamas F, Roundy D, Mikaelian G, Vitug G, Rudner M, Shih J, Smith D, Segura J and Khakoo M A 2000 Angular profiles of molecular beams from effusive tube sources: I. Experiment *Meas. Sci. Technol.* **11** 1750–65
- [18] Guevremont J M, Sheldon S and Zaera F 2000 Design and characterization of collimated effusive gas beam sources: effect of source dimensions and backing pressure on total flow and beam profile *Rev. Sci. Instrum.* **71** 3869–81
- [19] Blauner P G, Ro J S, Butt Y and Melngailis J 1989 Focused ion-beam fabrication of sub-micron gold structures *J. Vac. Sci. Technol. B* **7** 609–17
- [20] Scheuer V, Koops H and Tschudi T 1986 Electron beam decomposition of carbonyls on silicon *Microelectron. Eng.* **5** 423–30
- [21] Komuro M, Watanabe N and Hiroshima H 1990 Focused Ga Ion-beam etching of Si in chlorine gas *Japan. J. Appl. Phys. Part 1-Regular Pap. Short Notes Rev. Pap.* **29** 2288–91
- [22] Kohlmann K T, Thiemann M and Brunger W H 1991 E-Beam induced x-ray mask repair with optimized gas nozzle geometry *Microelectron. Eng.* **13** 279–82
- [23] El-Morsi M S, Wei A C, Nellis G F, Engelstad R L, Sijbrandij S, Stewart D and Mulders H 2004 Gas flow modeling for focused ion beam (FIB) repair processes *Proc. of SPIE—The Int. Society for Optical Engineering* ed W Staud and J T Weed (Monterey, CA) pp 467–76
- [24] Friedli V, Santschi C, Michler J, Hoffmann P and Utke I 2007 Mass sensor for *in situ* monitoring of focused ion and electron beam induced processes *Appl. Phys. Lett.* **90** 053106
- [25] Utke I, Friedli V, Amorosi S, Michler J and Hoffmann P 2006 Measurement and simulation of impinging precursor molecule distribution in focused particle beam deposition/etch systems *Microelectron. Eng.* **83** 1499–502
- [26] Roy S, Raju R, Chuang H F, Cruden B A and Meyyappan M 2003 Modeling gas flow through microchannels and nanopores *J. Appl. Phys.* **93** 4870–9
- [27] Clausing P 1971 Flow of highly rarefied gases through tubes of arbitrary length *J. Vac. Sci. Technol.* **8** 636
- [28] Friedli V 2009 <http://www.empa.ch/GISSimulator>
- [29] Smith C G and Lewin G 1966 Free molecular conductance of a cylindrical tube with wall sorption *J. Vac. Sci. Technol.* **3** 92
- [30] Lafferty J M 1998 *Foundations of Vacuum Science and Technology* (New York: Wiley)
- [31] Bird G A 1994 *Molecular Gas Dynamics and the Direct Simulation of Gas Flows* (Oxford: Clarendon)
- [32] Friedli V 2008 Focused electron- and ion-beam induced processes: *in situ* monitoring, analysis and modelling *PhD Thesis* Ecole Polytechnique Fédérale de Lausanne
- [33] Herman M A and Sitter H 1996 *Molecular beam Epitaxy Fundamentals and Current Status* (Berlin: Springer)
- [34] Thomson S L and Owens W R 1975 Survey of flow at low-pressures *Vacuum* **25** 151–6
- [35] Henderson M A, Ramsier R D and Yates J T 1991 Minimizing ultrahigh-vacuum wall reactions of Fe(Co)₅ by chemical pretreatment of the dosing system *J. Vac. Sci. Technol. a-Vac. Surf. Films* **9** 2785–7
- [36] Kudas T T and Hampden-Smith M J 1994 *The Chemistry of Metal CVD* (Weinheim: VCH)
- [37] West G A and Beeson K W 1988 Chemical vapor-deposition of cobalt silicide *Appl. Phys. Lett.* **53** 740–2
- [38] Kunz R R and Mayer T M 1988 Electron-beam induced surface nucleation and low-temperature decomposition of metal-carbonyls *J. Vac. Sci. Technol. B* **6** 1557–64
- [39] Garner M L, Chandra D and Lau K H 1995 Low-temperature vapor pressures of W-, Cr-, and Co-carbonyls *J. Phase Equilib.* **16** 24–9
- [40] Bret T, Utke I and Hoffmann P 2005 Influence of the beam scan direction during focused electron beam induced deposition of 3D nanostructures *Microelectron. Eng.* **78–79** 307–13
- [41] DeMarco A J and Melngailis J 1999 Lateral growth of focused ion beam deposited platinum for stencil mask repair *J. Vac. Sci. Technol. B* **17** 3154–7